PAPER

Check for updates

Composite cathode material for improved aluminum–polymer batteries

Shuvrodev Biswas, [ID] *[a] Thomas Köhler, [ID] [a] Amir Mohammad,[a] Hartmut Stöcker [ID] [a] and Dirk C. Meyer[a,b]

Rechargeable aluminum batteries (RABs) are an emerging post-lithium technology for their large ore reserves and better safety properties. However, conventional cathode materials like graphite have limited storage capacity because the intercalation of $AlCl_4^-$ occurs only in every third or fourth layer of graphite. On the other hand, organic compounds with a different working principle lack stability in the strongly Lewis acidic electrolytes due to rapid dissolution. Hence, this investigation presents a composite consisting of an organic compound 9,10-phenanthrenequinone (PQ) and graphite as a cathode material for improved RABs. For the melt diffusion synthesis, spherical graphite (SPG) was used at a ratio of 2 : 3 to PQ. A recently developed solid polymer based on aluminum chloride ($AlCl_3$), triethylamine hydrochloride (Et_3NHCl) and polyamide (PA6) was used as electrolyte. The combination of fabricated composite and solid polymer electrolyte (SPE) with an Al anode offered significant improvement in capacity and cyclability compared to pure SPG or pure PQ cathodes. The cyclic voltammetry analysis showed that both components contribute to the capacity, which was also confirmed by *operando* XRD, FT-IR, XPS, and EPR analysis. Therefore, both intercalation and coordination reactions take place synergetically. Additionally, SPG was exchanged with meso carbon micro-beads (MCMB) and graphite flakes (GF), which demonstrated no considerable impact of the graphite particle shape on the cathode performance.

Broader context

Rechargeable aluminum batteries have gained significant research interest due to their high theoretical capacity, safety, and material abundance. However, their widespread application is hindered by challenges such as cathode degradation, poor conductivity, and limited cycle life, primarily caused by the corrosive nature of electrolytes. Addressing these issues, a composite cathode material combining phenanthrenequinone (PQ) and graphite is proposed, which exhibits twice the conductivity and improved stability in solid polymer electrolytes. Our study reveals that PQ and graphite actively participate in the electrochemical process through two distinct mechanisms: the intercalation of $AlCl_4^-$ into graphite and the coordination reaction between PQ and $AlCl_2^+$. This collaborative interaction results in enhanced capacity, cyclability, and energy density, making aluminum polymer batteries an interesting option for next-generation batteries. Furthermore, the composite performs consistently across different graphite types, highlighting its adaptability. These advancements contribute to the broader goal of sustainable energy storage, offering a safer, more abundant, and cost-effective alternative to conventional battery technologies for future applications.

1. Introduction

In today's world, lithium-ion batteries (LiBs) are dominating the sector of rechargeable batteries due to their tremendous progress in performance. However, there are still some issues like safety concerns,[1] high costs of raw materials, *i.e.* lithium and cobalt,[2] and challenges like co-intercalation and the poor oxidative stability of conventional electrolytes[3] so that

researchers are looking for alternative chemistries beyond LiBs. Among all the potential replacements for LiBs, rechargeable aluminum batteries (RABs) have drawn immense attention for their availability (3rd most abundant element on earth), impressive theoretical volumetric (8056 mAh cm^{-3}), and gravimetric (2981 mAh g^{-1}) capacities considering a three-electrons process,[4] and comparatively safer chemistry.[5] Despite the exceptional properties exhibited by Al–metal anodes, the performance of rechargeable aluminum batteries (RABs) remains inadequate for practical commercial deployment.

One of the primary challenges is the fabrication of suitable cathodes that have sound compatibility with electrolytes[6] and facilitate multivalent Al ion storage. In particular, intercalating

[a]Institute of Experimental Physics, TU Bergakademie Freiberg, Leipziger Str. 23, 09599 Freiberg, Germany. E-mail: shuvrodev.biswas@physik.tu-freiberg.de
[b]Center for Efficient High-Temperature Material Conversion, TU Bergakademie Freiberg, Winklerstr. 5, 09599 Freiberg, Germany

the trivalent Al^{3+} ion into crystalline host structures poses inherent challenges attributable to the strong coulombic attractions within the anionic frameworks because of high activation energies.[7,8] The high activation energy promotes rapid complexation of Al^{3+} with ions like Cl^-, which inhibits its direct intercalation into the host structure. Therefore, instead of the preliminary assertion of having three electrons from a single Al atom, the most studied cathode graphite offers only 3 electrons from 8 Al atoms by the insertion of $AlCl_4^-$:[9,10]

$$Al + 7AlCl_4^- \leftrightarrow 4Al_2Cl_7^- + 3e^- \quad (1)$$
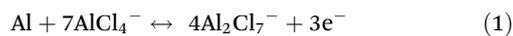
In the search for cathode materials with a higher number of transferred electrons, so far, only a few cathodes (*e.g.* V_2O_5 nanowires, TiO_2 nanotube arrays, MoS_2 microspheres, *etc.*) have been reported to intercalate Al^{3+} ions.[11–13] However, apart from the early-mentioned strong coulombic attractions, these materials also suffer from low electrical conductivity, lack of suitable electrolyte match, unwanted side reactions, rapid capacity fading, and limited cyclability.[14–16] In addition to the cathodes with intercalation mechanism, coordination reaction-based cathode materials, specifically organic materials like polycyclic aromatic hydrocarbons (PAH), conductive polymers, and tetradiketones are explored by several research groups because of their structural diversity and flexibility, sufficient intermolecular spaces to ease the strain management and storage of complex Al carrier ions, *e.g.* $AlCl^{2+}$ and $AlCl_2^+$.[17,18] For instance, anthraquinone,[19] 9,10-phenanthrenequinone,[20] tetradiketone,[21] and their derivatives have exhibited promising performance. Nonetheless, they are inhibited by rapid dissolution and low electrical conductivity, leading to poor cyclability and significant capacity loss. To resolve these challenges, a composite of 9,10-phenanthrenequinone and activated carbon,[22] poly(phenanthrenequinone) (pPQ),[23] polythiophene (PT),[24] a macrocycle of phenanthrenequinone or a hybrid of pPQ and graphite flakes (PQ-Δ-HY)[20] are potential research directions. Still issues like poor electrical conductivity, low nominal voltage, and the use of highly corrosive ionic liquid (IL) electrolytes persist.

In ionic liquid (IL) electrolytes, such as $AlCl_3 : Et_3NHCl$,[25] $AlCl_3 :$ pyridinium chloride,[26] $AlCl_3 :$ urea,[27] $AlCl_3 :$ 1-ethyl-3-methylimidazolium chloride ([EMIM]Cl),[28,29] $AlCl_3$–NaCl–KCl,[30] $AlCl_3$–NaCl–LiCl–KCl[31] the electrochemically active species $Al_2Cl_7^-$ acts as a source of anolytes for the electrochemical deposition of aluminum,[25,32] which is crucial for battery functioning. However, these electrolytes possess certain disadvantages, especially their extremely corrosive nature and susceptibility to moisture, impacting both coulombic efficiency and cycling stability.[33] As a result, these limitations curtail the commercialization of aluminum batteries in large-scale energy storage. Addressing these issues, IL-based polymer electrolytes were introduced, which can lower moisture sensitivity, and electrolyte leakage and also enable separator-free RABs.[34–37] In one of our recent studies, we presented an iono-polymer electrolyte based on polyamide (PA6)[38] with

some promising results; however, the capacity with spherical graphite cathodes is still compromised.

Herein, addressing all the above points, this study presents a composite cathode material based on PQ and SPG synthesized by a one-step melt diffusion process for RABs using an $Et_3NHCl : AlCl_3$-based solid polymer electrolyte (see Fig. S1, SI). The iono-polymer electrolyte is flexible, easy to prepare, and suitable for commercial cell housings because of reduced leakage and corrosivity.[38] With this approach, the capacity ($C_{cathode}$) can be increased with a higher nominal voltage, *i.e.* better energy density compared to the individual components. Moreover, we propose a combination of coordination and intercalation ion transfer mechanisms supported by *operando* X-ray diffraction (XRD), Fourier transform infrared spectroscopy (FT-IR), X-ray photoelectron spectroscopy (XPS), electron spin resonance spectroscopy (ESR) and cyclic voltammetry (CV). Considering the variation in electrochemical performance associated with the morphology of different graphite forms,[39] we investigate their role as host materials for PQ in RABs. Additionally, the effect of temperature on the performance of RABs using SPE is explored.

2. Results and discussion

2.1. Properties of the composites

The composite formed a mold like the shape of the container after heat treatment (see Fig. S1a, SI), which was the first indication of a successful fabrication through melt diffusion, because melted PQ worked as a binder for the graphite particles. To study the changes in surface morphology, concentric backscattered electron microscopy (CBS) analysis was done using a FEI Helios Nanolab 600i with an acceleration voltage of 10 kV and a current of 69 nA. The study shows that the composite shown in Fig. 1d had no shape like its components (Fig. 1a and b). Although the milling process could potentially influence this disparity, Fig. 1c suggests otherwise. The ball milling does not appear to significantly alter the particle shapes, as evidenced in Fig. 1c. However, a slight deformation of the SPG particles is noticeable, particularly in the inset of Fig. 1c. Hence, the considerable explanation is that the PQ particles completely melt and adhere to the surface of the deformed graphite particles during the melt diffusion process. As a result, the composite particles exhibit smooth surfaces, in contrast to the layered structure of the graphite particles (compare Fig. 1b and d with inset). Such smooth surfaces of the particles confirm a well-synthesized composite, which is also claimed by Yoo *et al.* for their composite of activated carbon and PQ.[22]

To determine the quantity of PQ present in the SPGPQ composite material, a thermogravimetric analysis (TGA) was conducted under argon atmosphere using a Setaram TGDSC + IR 120523. The samples (4.5 mg of each) were heated from room temperature to 600 °C at a heating rate of 10 K min^{-1}. Fig. 1e shows the TGA analysis of an SPGPQ composite sample and the two starting materials (pure PQ and SPG powder). It can
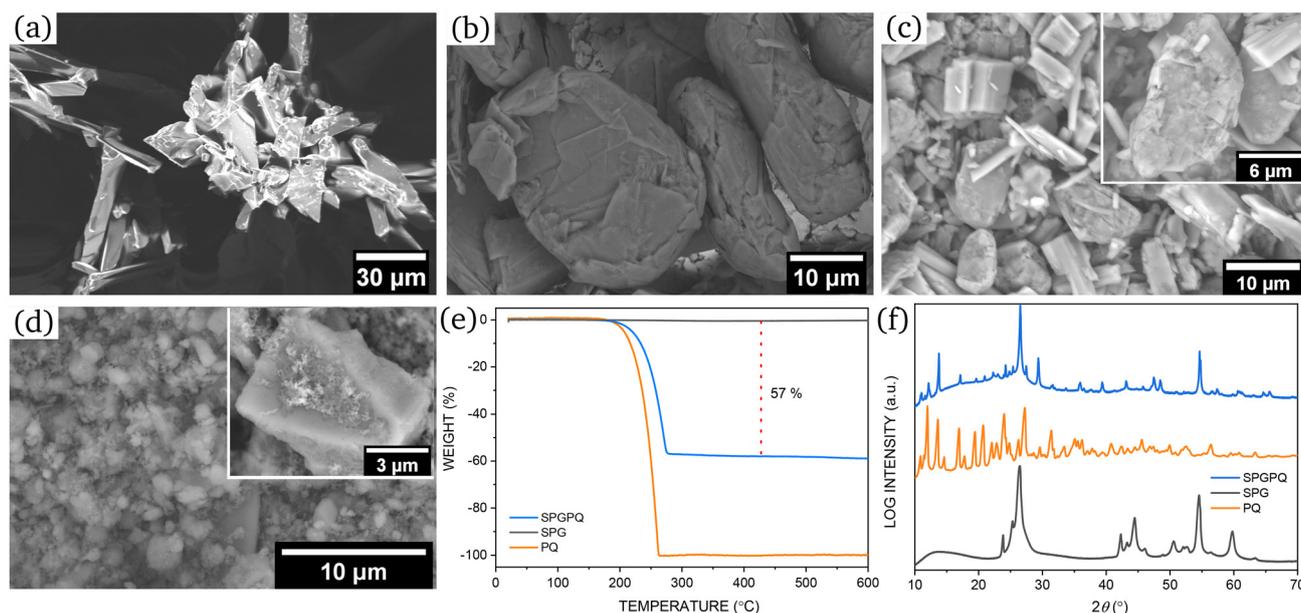
Fig. 1 Comparison between properties of SPGPQ and its components: CBS images of (a) PQ, (b) SPG, (c) SPGPQ composite (after 30 min of milling), inset: slightly deformed particles, (d) SPGPQ composite (after melt diffusion), inset: smooth surface of one particle indicating the composite formation, (e) TGA analysis, and (f) XRD of all materials.

be seen that the pure PQ powder is completely vaporized at around 260 °C (melting temperature 206 °C). In comparison, there is no change in the pure SPG powder. On the other hand, the composite material shows a weight loss of around 57% at approximately 270 °C. From this, it can be concluded that the PQ has completely evaporated and the composite consists of approx. 43 wt% graphite (close to a 3 : 2 ratio).

The powder diffraction patterns of the composite are also different from the diffraction patterns of PQ and SPG. Fig. 1f shows that diffractions of PQ either disappeared or shifted after the formation of the composite due to the reduction of crystallinity. The reflections that could be attributed to PQ, such as those at $2\theta = 12°$, $14°$, $20°$, and $24°$, were also significantly suppressed in intensity. Similar trends are also observed at higher angles. Such reduced crystallinity is also reported for PQ composites with activated carbon.[22] The intensity of graphite 002 reflection in the composite was also significantly decreased compared to pure graphite. This characteristic can be attributed to the coating of the PQ onto the graphite particles or the partial reduction of graphite to graphene oxides due to annealing at 250 °C.[40,41] The position (26.4°) and width of the reflection is almost similar to the reflection of pristine SPG, implying that SPG particles were functioning well as hosts for the PQ melts.

2.2. Stability of the composite in the electrolyte

The stability of the composite and its components in solid polymer electrolytes was investigated *via* attenuated total reflection (ATR) in the infrared range (FT-IR spectroscopy). PQ and SPGPQ electrodes were kept in contact with the electrolyte for 5 min and 30 min to analyze the caused changes. Fig. 2a

and b show that the pure PQ electrode is unstable in the ionic polymer and reacts over time. The FT-IR spectra of the PQ without air contact show clear differences for 5 min and 30 min and longer time led to more pronounced changes in the IR spectra. Particularly, the change in the spectral range of the carbonyl stretching vibration (ν C=O) shows a clear shift from 1673 cm^{-1} to 1542 cm^{-1}. This shift can be attributed to the complexation of AlCl$_x$ species at the electroactive C=O group, forming a C=O–[AlCl$_x$]$^{3-x}$ complex.[19,23,42]

In addition, broad and prominent vibrational modes are observed at 762 cm^{-1} and 483 cm^{-1}, whereby the former could have its origin in the bending vibration of the new carbonyl complex and the latter could be assigned to adsorbed electrolyte residues. The latter is plausible, as it is the typical vibrational range of species like ν AlCl$_4^-$ and ν Al$_2$Cl$_7^-$.[38] The other vibrational modes, for example, the bending vibration δ C–H–C and δ C–C–C at 1120–1163 cm^{-1} and 1230–1333 cm^{-1} respectively, are reduced in intensity. It is seen that the δ C-ring mode (763 cm^{-1}) and ν C=C (1450 cm^{-1}) intensity are almost unchanged, which confirms the statement about complexation only in the carbonyl group. This observation indicates a purely chemical, rather than electrochemical, interaction with the electrolyte under an Ar atmosphere, which is unfavorable for stable battery performance.

Interestingly, the vibration modes exhibit recovery upon air contact, and within approximately 150 s the spectrum of the C=O stretching vibrational mode is almost restored. In both cases, similar characteristics are observed. Such observation suggests that the complexation is limited to the surface and happens with a highly reactive and transient species, which interacts rapidly with air and then decomposes.
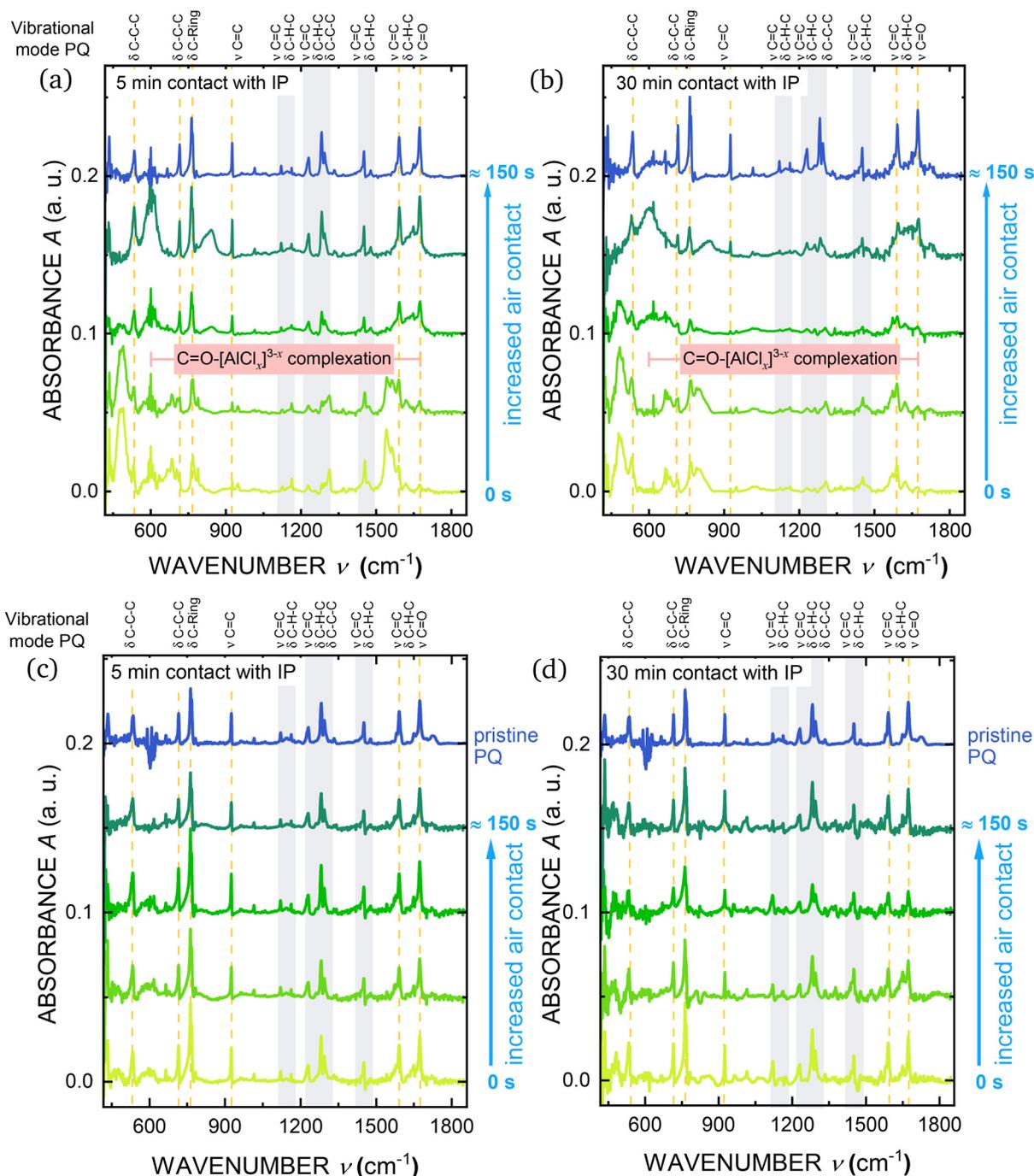
Fig. 2 FT-IR spectra comparison showing the stability of electrodes in SPE: PQ electrodes after (a) 5 min and (b) 30 min of contact; SPGPQ composite electrodes after (c) 5 min and (d) 30 min of contact with the spectrum of the pristine PQ cathode shown at the top (blue). The vibration modes of pure PQ are indicated.

The behavior of the composite SPGPQ is quite stable (see Fig. 2c and d) with no significant spectral changes observed even after 30 min of contact with the electrolyte. The strong resemblance of these SPGPQ spectra to that of the pristine PQ cathode (shown in blue at the top of Fig. 2c and d), is a clear indication of a successful synthesis and the enhanced chemical stability against the strong Lewis acid.

The $C{=}O{-}[AlCl_x]^{3-x}$ complexation is also absent, so that there are no changes in the relevant PQ vibration modes, *i.e.* $C{=}C$ and $C{=}O$, while the sample was exposed to air. This confirms that the composite avoids the undesirable chemical interaction seen in pure PQ, making it a more suitable cathode material for reversible electrochemical processes in batteries.

2.3. Ion transfer mechanism

2.3.1. Intercalation of AlCl$_4^-$ species. Fig. 3a shows the diffraction pattern of a cell with SPG cathode with a voltage-time plot during charging and discharging. The 5th cycle is considered for analyzing the data compared to the diffraction pattern of the as-prepared cell. It is clearly seen that the graphite 002 reflection is partly shifted with the increase of voltage while charging and at 2.35 V, when the cell is completely charged, there are 3 reflections at 2θ of 20.7°, 26.6°, and 27.8° for the SPG cathode. The observed peak shifting and emergence of new peaks are in good agreement with the literature.[29,43] The persistent reflection at 26.6° may be attributed to inactive graphite material.

The XRD data suggest well-defined staging and long-range order in the anion-graphite intercalation structures, comparable to stage-4 intercalation of AlCl$_4^-$ into graphite at room temperature, as suggested by Pan *et al.*[44] The reflections at 20.7° and 27.6° gradually emerge while charging, whereas the original reflection at 26.6° is losing some intensity. This development can be attributed to a structural evolution of graphite from stage n to stage $n − 1$ (n = integer; corresponding to one layer of ions for every n graphene layers) of the AlCl$_4^-$ intercalated SPG compound.[44,45] This means at stage-4 during charging >2 V, when AlCl$_4^-$ ions intercalate into graphite, they force the layers apart, leading to a new reflection at 20.7°, caused by periodically inserted AlCl$_4^-$ ions. At the same time,

a partial peak shift towards higher angles results from the compression of non-intercalated layers.

Fig. 3b shows the changes in diffraction pattern over time during charging and discharging over 14 cycles. A repetitive pattern can be observed during discharging; however, it does not return exactly to its pristine state, probably due to residual disorder and strain, which could be attributed to an irreversible reaction process. Although the peak intensity at 26.6° is reduced at the end of charging, it is still dominating. The partial but consistent peak shifting towards higher angles for every charged state (2.35 V) and returning to its initial state at 0.5 V indicates a high degree of reversibility of the intercalation–deintercalation process even though the graphite structures were not restored completely. The structural analysis also suggests a continuous structural compression and elongation along the c-axis from 6.4 Å (charging) to 6.7 Å (discharging), which is similar to previous studies.[30,43]

In Fig. 3c, the diffraction pattern of the SPGPQ composite cathode during cell cycling is shown. The organic PQ does not show any distinct diffraction peaks other than the characteristic peak of graphite at 26.6°. This indicates that the complexation of PQ with AlCl$_3$-based ions has converted PQ to an amorphous phase. From the FT-IR analysis, it is observed that complexation reactions take place between C=O of PQ and $[AlCl_x]^{3-x}$ when they come into contact, which could result in such an amorphous state (see Fig. 3c and d). Therefore, the crystallinity of PQ likely does not play a signifi-
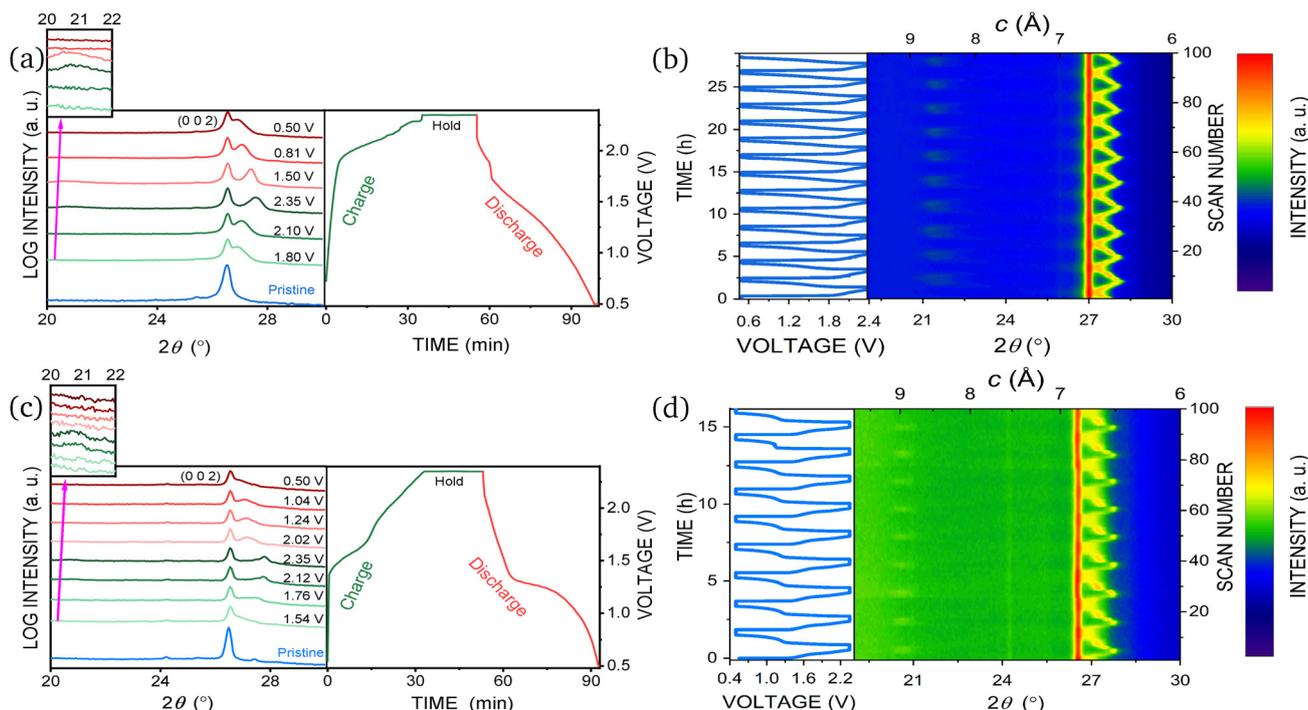

Fig. 3 *Operando* XRD study of AlCl$_4^-$ intercalation: (a) diffraction patterns of a cell with SPG cathode combined with voltage time curve for 5th cycle, inset: zoom-in of the reflection at 2θ = 20°−22°, (b) contour plot of the same cell for 14 cycles with the changes in c-axis of the graphite structure, (c) diffraction patterns of a cell with SPGPQ composite cathode with voltage-time curve, inset: zoom-in of the peak at 2θ = 20°−22° and (d) contour plot of the same cell for 9 cycles with the changes in c-axis of the graphite structure.

cant role in the electrochemical process. In addition, the amorphization of PQ could be advantageous in resisting phase transition and dissolution, and enhancing stability, which implies enhanced cyclability.[20,22] Although the intensity of the graphite 002 reflection in SPGPQ is weaker than for the pure SPG cathode, a similar trend of peak shifting and new peak emerging is observed during cycling. This strongly supports the hypothesis of the graphite contributing to electrochemical reactions (intercalation) also for composite cathodes. In this case, the peak shifts to a slightly higher angle of 27.8° compared to the SPG cathode with 27.6°. The stable reversibility of intercalation–deintercalation can also be confirmed from Fig. 3d, *i.e.* the composite cathode behaves similar to SPG.

2.3.2. FT-IR analysis. Like all n-type compounds that accept electrons and become negatively charged during discharge, C=O, the electroactive functional group of PQ, is reduced during discharge and interacts with $Al_2Cl_7^-$. There are different opinions in the literature about the coordinating chloroaluminate complexes, for example, $AlCl_2^+$ [20,46,47] and $AlCl^{2+}$,[19,23,42] which influences the achievable capacity of the cathodes accordingly. To investigate the reaction mechanism, ATR-FTIR spectroscopy is carried out on different states of the solid polymer RABs with SPGPQ cathodes. In this case, the IR spectra of pristine SPGPQ and cells after charge–discharge, discharge–charge–discharge, after the first charge and the 25th charge are recorded (see Fig. 4) to have a clear understanding of the mechanism and reversibility.

The spectrum of the pristine SPGPQ composite is dominated by the stretching vibrations and bending vibrations of the ring compound consisting of C=C and C–H–C groups. The stretching vibration of the carbonyl bond C=O, the characteristic mode of quinone is found at 1673 cm^{-1}.[48] After the first charge (2.35 V), the characteristic peak at 1673 cm^{-1} disappears and a new broad and dominant peak appears at 1536 cm^{-1} (see Fig. 4b), which can be attributed to the interaction between the electroactive carbonyl group and the $Al_2Cl_7^-$. This could be the stretching vibration of a new complex of the carbonyl group C=O–$[AlCl_x]^{3-x}$ ($0 < x < 3$). A couple of other peaks observed around 1314 cm^{-1} can also be attributed to such complexation[19] (see Fig. 4c).

Both the discharged spectra at a voltage of 0.5 V show a distinct difference compared to the charged state. The vibrational modes at 1536 cm^{-1} and 1314 cm^{-1} entirely disappear and a doublet of new vibration modes at 1337 cm^{-1} and 1350 cm^{-1} increase prominently, which can be assigned to the stretching vibration of C–O (see Fig. 4c).[23] This phenomenon suggests that the interactions between the C=O group of quinone and $AlCl_x$ complexes change the vibrational modes and never return to their initial state. The new peaks at 1337 cm^{-1} and 1350 cm^{-1} reflect the electron transfer process during discharge, where C=O is reduced to C–O.

Furthermore, the spectrum of a charged cathode after the 25th cycle produced almost a similar spectrum to the charged cathode after the first charge indicating the high reversibility of the complexation reaction. The ratio of the integrated area
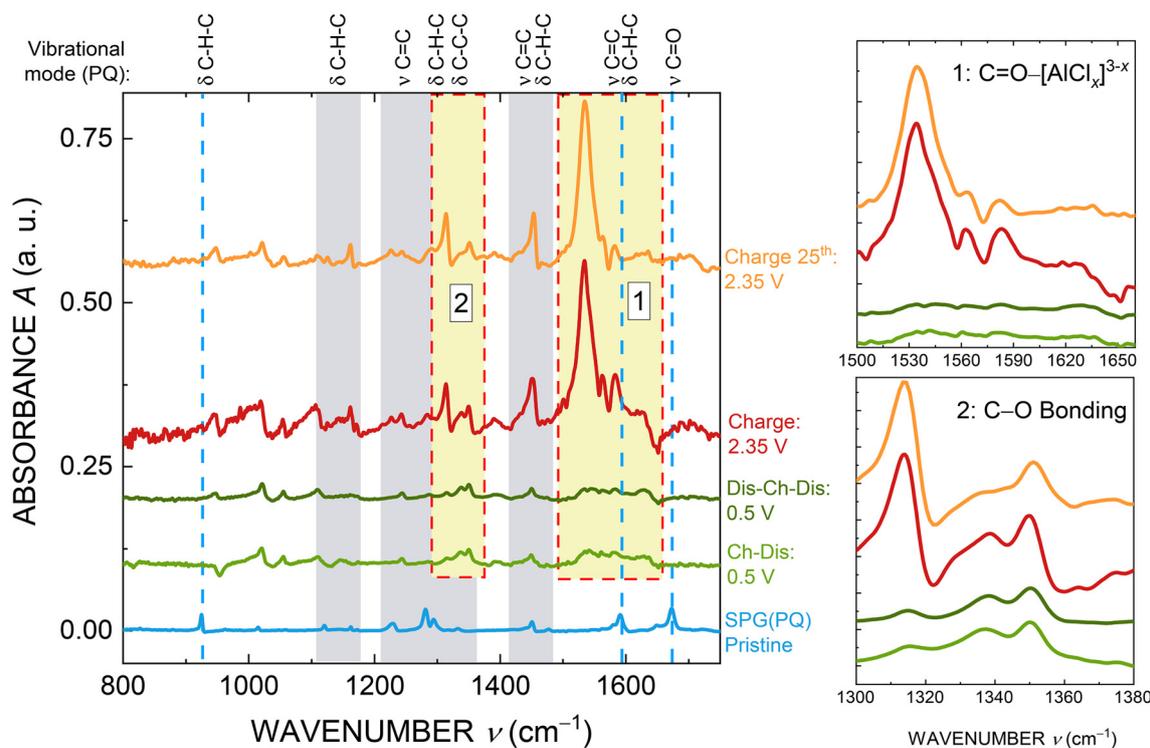

Fig. 4 FTIR spectra of the SPGPQ composite at different states of cycling: (a) full spectra, (b) magnified portion for C=O–$[AlCl_x]^{3-x}$ complexation and (c) magnified portion for C–O formation during discharging.

of the broad peaks at 1536 cm^{-1} (see Fig. 4b) of the two charged states is ≈94%, which also suggests a highly reversible complexation process with minimal irreversibility. This observation highlights the consistent appearance of the peak for C=O–[AlCl$_x$]$^{3-x}$ complexation while charging and decomplexation during discharging after multiple charge and discharge cycles. The slight decrease in the integrated area could be caused by some minor side reactions or slow decomposition of PQ and SPGPQ. However, the analysis evidently supports that the core electrochemical processes are highly reversible, which is crucial for the long-term stability and efficiency of the battery.

2.3.3. X-ray photoelectron spectroscopy (XPS) analysis. The XPS peak shift provides practical insight into the binding structures of the charge carrier ions. This is due to the sensitivity of the binding energy of the core electrons to the chemical environment of the corresponding element. For this, *ex situ* XPS measurements of pristine, fully charged and fully discharged SPGPQ cathodes were performed. It is noteworthy that all XPS peaks were referenced relative to the C–C bond at 284.8 eV in the C 1s branch. The individual spectra of O 1s, C 1s, Al 2p and Cl 2p with fitting curves are illustrated in Fig. 5. Fig. S2 in the SI shows the survey spectra and pristine O 1s and C 1s. The O 1s spectrum of the pristine SPGPQ (see Fig. S2c) is deconvoluted into peaks at 532.3 eV, 533.7 eV and 534.3 eV, which can be assigned to C=O (carbonyl group of PQ), C–O, and C–OH.[19,49] The carbonyl group is dominating in the charged state and decreasing significantly, when comple-

tely discharged (see Fig. 5a). This can be attributed to the formation of C=O–[AlCl$_x$]$^{3-x}$ through a coordination reaction. The fully charged state exhibits slightly broader peaks compared to the pristine state (see Fig. S2c) probably due to the presence of AlCl$_x$ species, *i.e.* C=O–[AlCl$_x$]$^{3-x}$. This is in agreement with the FT-IR results in the previous section.

Significant changes are observed in the C 1s spectra. Spectra in the pristine sample (see Fig. S2b, SI) do not have any shoulder or doublet, where C=O or C–C, C–O, C–H and C=O would be located at 284.7 eV, 285.6 eV, 286.9 eV and 288.6 eV, respectively.[21,50] The charged state develops a broader and more prominent shoulder at a higher binding energy of 286.3 eV. This could be a result of the electrochemical oxidation of graphite by the intercalation of AlCl$_4^-$,[29] which is reduced when discharged (see Fig. 5b). However, it does not return to its initial state.

More insights into ion species can be obtained from the Cl 2p (199.3 eV for 2 p$_{2/3}$ and 200.9 eV for 2 p$_{1/3}$) and Al 2p (75.6 eV) spectra, where the intensity in the charged state was significantly higher than the discharged state. The calculated atomic concentration ratios of Al and Cl are approximately 1 : 4 in the charged state and 1 : 2.2 in the discharged state. These ratios suggest that AlCl$_4^-$ species dominate in the charged state, which is consistent with the intercalation of AlCl$_4^-$ into graphite layers. In the discharged state, the possible ionic compound is AlCl$_2^+$, indicating the coordination reaction accompanied by a one-electron transfer process, likely involving the formation of C=O–[AlCl$_x$]$^{3-x}$ complexation. Energy
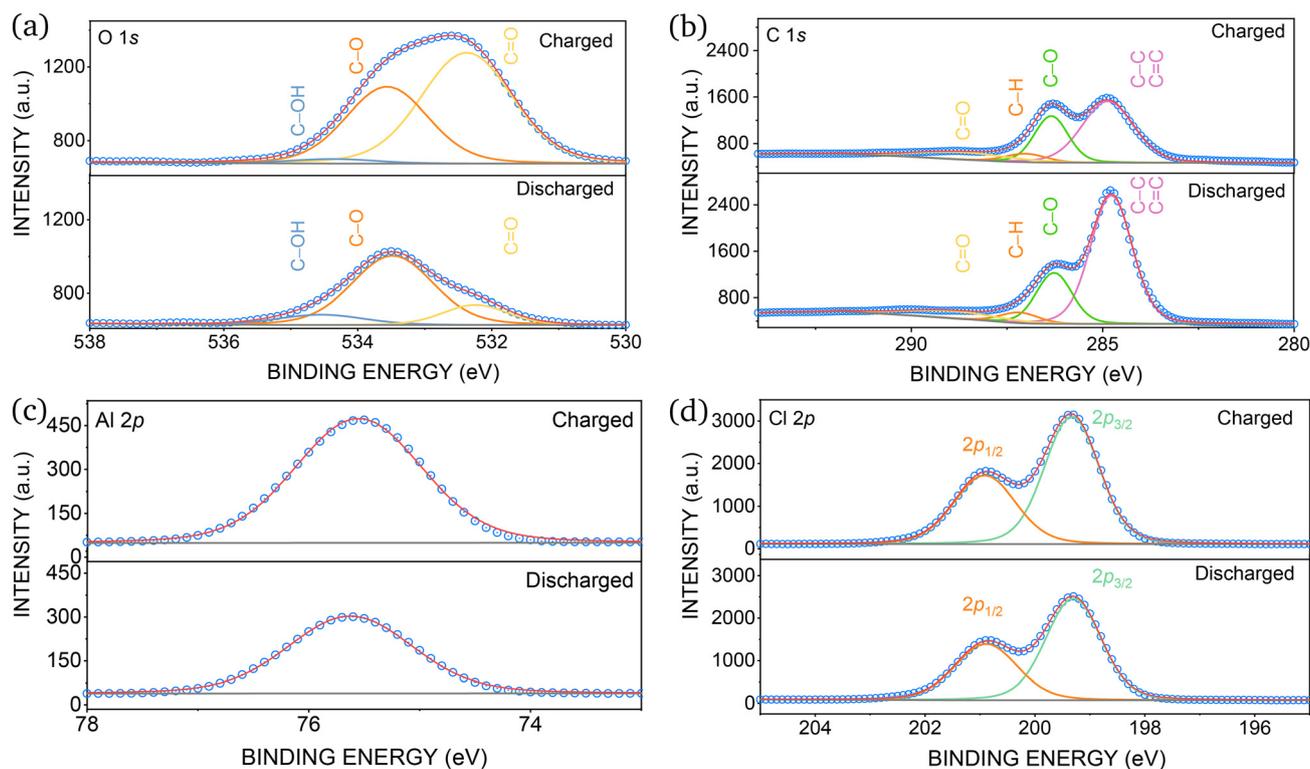

Fig. 5 XPS spectra of elements for charged and discharged state of the SPGPQ cathode with fitting curve: (a) O 1s, (b) C 1s, (c) Al 2p and (d) Cl 2p.

dispersive X-ray spectroscopy (EDS) analysis at multiple points (see Fig. S3, SI) reveals atomic ratios of $1:3.8$ in the charged state and $1:2.0$ in the discharged state, as shown in Table S2 (SI), further corroborating this finding. A similar ratio is also reported by Yoo *et al.*[21] and Mao *et al.*[47]
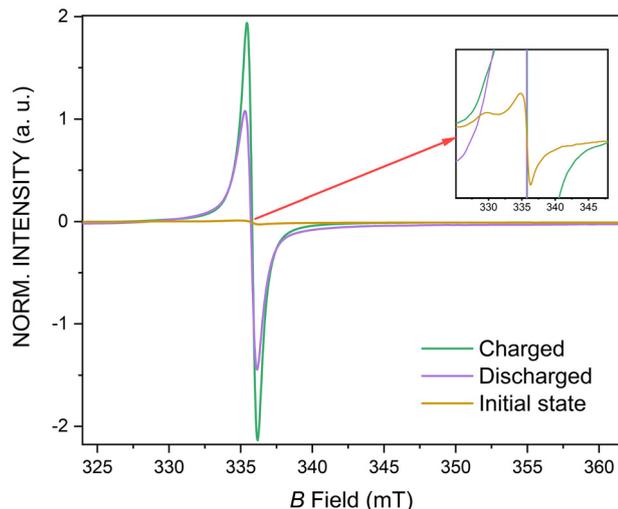

Fig. 6 ESR analysis of initial, charged and discharged state of an SPGPQ cathode normalized to sample mass, inset: a magnified view of the initial state spectrum.

2.3.4. Electron spin resonance (ESR) analysis. ESR spectra of the samples were recorded, as depicted in Fig. 6. All treated composites and the pristine state exhibit a signal close to the free electron of approximately $g_e = 2.004$. The untreated SPGPQ composite displays only a very weak signal, which possesses the well-known shape of graphitic material with its anisotropic g_e value (see Fig. 6 inset).[51]

Conversely, the loaded and unloaded composite materials exhibit a large signal, attributable to the accommodation of charges. During the charging process, $AlCl_4^-$ is intercalated into the graphite; due to the reversibility of this process, this signal should be significantly reduced upon discharging. However, this is not the case, but almost an equally large area (3.8992 at 2.35 V after fully charged and 3.6429 at 0.5 V after fully discharged) under the ESR signal is detected. This confirms the FTIR results, indicating the formation of radical states due to complexation processes involving the carbonyl group of PQ upon contact with the electrolyte. Both the $C=O–[AlCl_x]^{3-x}$ complexation and $C–O–AlCl_2^+$ coordination are ESR-active. In the discharged state, only one electron per molecular unit of PQ is available, which explains the resulting spectral shape. This means the one-electron transfer process of PQ is preferable, which is also supported by the XPS analysis.[20,22]

2.4. Electrochemical analysis

2.4.1. Reaction kinetics. Fig. 7 a shows the CV curves comparing PQ, SPG, and SPGPQ at a scan rate of 1 mV s^{-1}, where
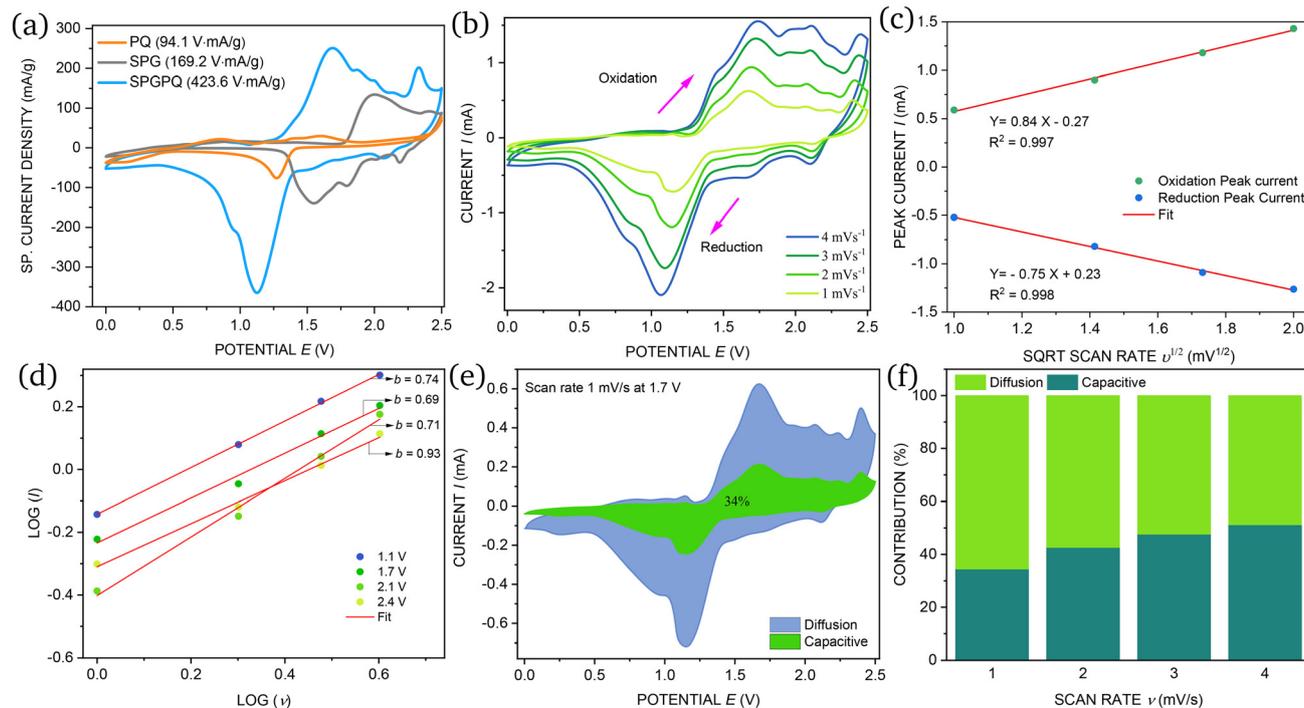

Fig. 7 Reaction kinetics analysis of the composite electrodes: (a) comparison of CV curves between SPGPQ and its components at 1 mV s^{-1} with integrated area given in the legend, (b) scan-rate dependency of the composite cathode, (c) the relation between peak currents and the square root of scan rates, (d) calculation of *b* values at different peak positions, (e) contribution of capacitive and diffusion current at 1 mV s^{-1}, and (f) current contribution at different scan rates.

the specific (sp.) current density is calculated using the active mass of the cathode. The CV curves have multiple oxidation and reduction peaks, and the composite offers a significantly higher sp. current density compared to its components. In the case of SPGPQ, the peaks are merged, suggesting that both graphite and PQ contribute synergistically to the electrochemical reaction kinetics, similar to previously reported PQ composites.[20] This merging of peaks in SPGPQ enables the possibility of a wider voltage window for charging and discharging, which is advantageous for enhanced battery performance. When comparing the peak positions across all curves, it becomes evident that the fabricated composite offers a wider functional charge–discharge window (2.35 V–0.5 V) compared to PQ (1.8 V–0.2 V) and SPG (2.35 V–0.8 V).

Notably, the primary oxidation peak of SPGPQ occurs at 1.6 V with a sp. current density of ≈240 mA g^{-1}, while the corresponding reduction peak is observed at ≈1.2 V with a higher sp. current density of 364 mA g^{-1}. The ratio of the reduction (190.7 V mA g^{-1}) and oxidation (188.4 V mA g^{-1}) area is nearly 1, which suggests excellent reversibility with high efficiency. The composite also has a remarkably higher integrated CV area (423.6 V mA g^{-1}) than the sum of CV areas of its components (263.3 mA g^{-1}). The calculated capacity of SPGPQ cathode based on the integrated area is 1.6 times higher than the combined capacity (see Fig. 7a). Such an increase in CV capacity could be attributed to the synergistic contribution of its components.

In addition, the increased surface area due to changes in shape and surface morphology during annealing (see Fig. 1d) may also result in more active sites for electrochemical reactions. This enhanced surface area would facilitate better ion accessibility and shorter diffusion pathways, resulting in efficient charge storage and higher capacity. The significantly increased conductivity of the composite electrodes (1.36 S m^{-1}) compared to PQ (0.56 S m^{-1}) (see Table 1) suggests better electrical pathways and reduced resistance, which ensures faster electron transfer. This also decreases the energy loss, supporting higher current density and contributing to a higher overall performance.

A scan rate-dependent CV measurement of a full RAB with SPGPQ cathode was carried out from 1 mV s^{-1} to 4 mV s^{-1} (see Fig. 7b) to elucidate the current contributions. The peak currents increased gradually with increasing sweep rate, with a slight peak shift from 1.67 V at 1 mV s^{-1} to 1.73 V at 4 mV s^{-1} (anodic) and from 1.14 V at 1 mV s^{-1} to 1.06 V at 4 mV s^{-1} (cathodic), while peak shapes remained unchanged. This

phenomenon can be attributed to a partial diffusion-controlled current with mostly reversible behavior. Peak currents are proportional to the square root of the sweep rate with an impressive R^2 value >0.99 for both anodic and cathodic reactions, which suggests high reversibility (see Fig. 7c). Further analysis using the power law

$$i = a\nu^b \tag{2}$$

at different peak positions and constant voltage shows that the b values differ from 0.7 to 0.9 (see Fig. 7d). Here, i is current, ν is scan rate and a, b are adjustable constants.[52] There are two well-defined conditions, where b = 0.5 signifies an ideal diffusion-controlled current contribution and b = 1 represents an ideal capacitive response. Therefore, the b value between 0.7 and 0.9 means the RAB with SPGPQ is a partial diffusion-controlled system, which is similar to pure PQ and also well-aligned with Yoo et $al.$[22] To separate the individual contributions to the reaction kinetics a simplified equation

$$i = k_1\nu + k_2\nu^{1/2} \tag{3}$$

is used, where $k_1\nu$ is capacitive current and $k_2\nu^{1/2}$ is diffusion controlled current.[52] Fig. 7e indicates that, at a scan rate of 1 mV s^{-1}, the diffusion current contributes 66% of the total current, with the remaining 34% attributed to the capacitive current. However, as the scan rate increases, the capacitive current gradually rises from 34% to 48% (see Fig. 7f), signifying accelerated reaction kinetics.[53,54]

2.4.2. Battery performance. RAB coin cells with composite, pure PQ, and SPG cathodes were cycled at 25 mA g^{-1} to evaluate the improvement of the SPGPQ performance compared to its components (see Fig. 8a). The cut-off charging and discharging voltages were set based on the CV analysis and the specific capacity is calculated considering the mass of active material of the cathode (see Table S1, SI). SPGPQ offers a capacity of 80 mAh g^{-1}, which is higher than the individual component capacity of PQ (46 mAh g^{-1}) and SPG (48 mAh g^{-1}).

However, the theoretical capacity of SPG (70 mAh g^{-1}) and PQ (129 mAh g^{-1}, for 1 electron process and 257 mAh g^{-1} for 2 electron process) mentioned in the SI are much higher than the experimental values. The discrepancy could be due to the partial inactivity of the active materials during cycling of the batteries with SPE. Moreover, the lower ionic conductivity of the SPE (0.3 mS cm^{-1})[38] than the IL (12 mS cm^{-1})[55] could be an influencing factor.

Table 1 Electrode conductivity and performance of different cathodes with only SPE at 25 mA g^{-1}

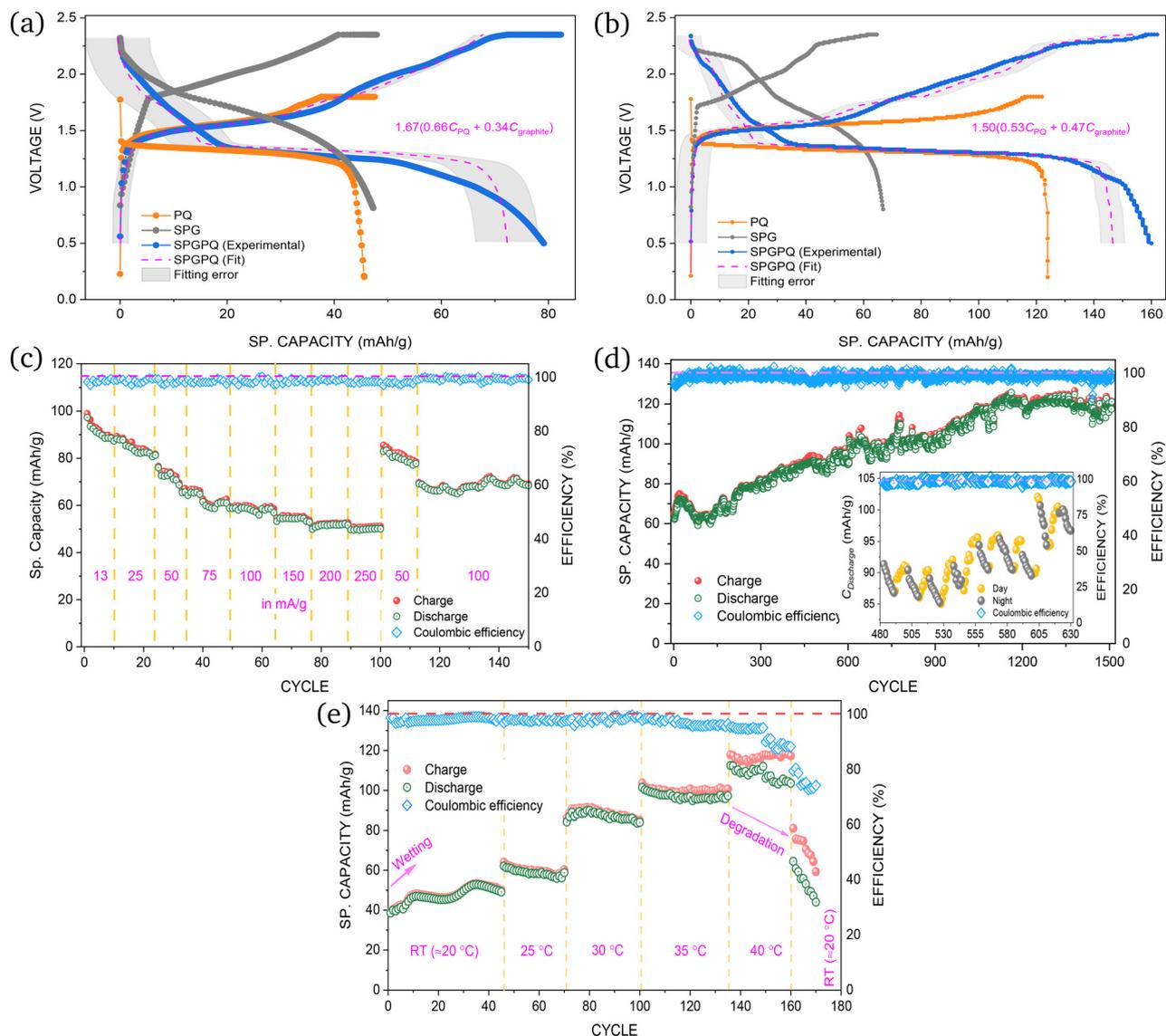| Cathode	Conductivity ± SD (S m^{-1})	Maximum $C_{cathode}$ (mAh g^{-1})	Capacity retention (%, after cycle 75)	coulombic efficiency (%, after cycle 75)	Energy density (Wh kg^{-1})
PQ	0.56 ± 0.02	45.6	70	44	64
SPG	5.43 ± 0.80	47.4	99	99	66
GFPQ	1.24 ± 0.04	88.0	87	90	119
SPGPQ	1.36 ± 0.04	79.2	99	99	111
MCMBPQ	0.92 ± 0.08	86.4	87	97	121

Fig. 8 Electrochemical performance of SPGPQ cathodes: (a) voltage profile of SPGPQ and its components over capacity with fit, (b) discharge capacities and fit with wetted cathodes, (c) rate-capability of capacity at different current densities, (d) capacities and coulombic efficiency over cycle number; inset: fluctuation in discharge capacity during day and night, and (e) temperature dependency on the capacity at 180 mA g^{-1}.

To test the hypothesis, different aluminum polymer batteries were cycled with ionic liquid wetted cathodes under similar conditions, ensuring the better utilization of the active materials. In this case, 5 µL of 2 : 1 AlCl$_3$/Et$_3$NHCl IL were used to wet each of the cathodes before cycling at 25 mA g^{-1}. The results, shown in Fig. 8b, exhibit significantly higher capacities for all of the cathodes, with near theoretical values of SPG and PQ cathodes. These results validate the hypothesis that wetting of the cathodes enhances active material utilization. However, the capacity of the wet PQ cathode with SPE dropped drastically after the first cycle compared to the cell without wetting (see Fig. S4, SI) due to faster dissolution of PQ.[19] Although the wet SPG cathode offers slightly better capacity, CE decreases to 90% (see Fig. S4c, SI), which is lower than that of the cell with

only SPE. A similar trend is observed for the wet composite cathode. Both the composite and its components offer poor cyclability when the cathodes were wet.

A closer inspection of the plateau of the curves in Fig. 8a reveals a synergistic effect in the case of SPGPQ. After a sharp increase of the voltage from 0.5 V to 1.7 V, SPG offers a broad and gradual charge plateau (grey curve), which starts at 4 mAh g^{-1} and increases to 47 mAh g^{-1} during charging, suggesting the intercalation of AlCl$_4^-$. On the other hand, the discharge voltage is around 1.8 V as the capacity approaches 46 mAh g^{-1} until the cut-off voltage of 0.5 V. PQ shows a much more stable plateau (1.4 V–1.2 V) throughout its capacity until a sudden voltage drop at around 44 mAh g^{-1} during discharge is caused by concentration polarization and over-potential.[56]

The voltage of PQ during charging reaches its cut-off voltage at a steady pace.

The composite (blue curve) follows both of the trends. It starts its plateau at around 1.4 V and imitates the consistent behavior of PQ delivering a specific capacity of 44 mAh g^{-1} during charging. At 1.7 V, it has a similar pattern to pure SPG with an extended capacity of 80 mAh g^{-1}. The combined properties are also well visible during discharging. Moreover, there is no sharp fall in capacity like for PQ cathodes; rather it reaches its cut-off voltage more steadily from 50 mAh g^{-1} at 1.3 V to 80 mAh g^{-1} at 0.5 V. Therefore, the composite incorporates the advantages of both SPG and PQ, resulting in improved performance and efficiency.

Based on CV and GCPL results, it is evident that both of the components are actively taking part in the electrochemical processes. The XRD analysis and spectroscopic results (XPS, FTIR, ESR) also support that both intercalation and coordination reaction are happening synergistically. To quantify the contribution of PQ and SPG to the composite overall capacity, a curve-fitting approach is employed using a simple linear combination model as a function of voltage:

$$C_{SPGPQ} = y \cdot [x \cdot C_{PQ} + (1 - x) \cdot C_{SPG}] \qquad (4)$$

Here, x signifies the fractional contribution of PQ, $(1 - x)$ is the contribution of SPG, and y is a performance enhancement factor describing the synergistic effects in the composite. The fitting analysis predicts the charge and discharge capacities of SPGPQ with SPE to be 72 mAh g^{-1}, having an average of $\bar{x} = 0.660 \pm 0.011$ and $\bar{y} = 1.668 \pm 0.009$ (see Fig. 8a). The enhancement factor suggests that the composite fabrication activates one or both components, potentially enhancing the kinetics and improving utilization of active sites or ion diffusion pathways. The results demonstrate a firm alignment with the fitting values derived from the RABs having wetted cathodes (see Fig. 8b), where $\bar{x} = 0.526 \pm 0.007$ and $\bar{y} = 1.502 \pm 0.014$, thereby validating the methodological approach employed. The details of the fractional contribution of PQ (x) and enhancement factor (y) are presented in the SI, Table S3. Changes in x may influence the specific capacity. Higher x values could shift the charge–discharge plateau toward that of PQ, while lower x values may align it more closely with SPG. Such adjustments could provide a balance between capacity, cyclability, and structural integrity of the composite.

Furthermore, the analysis indicates that PQ and SPG contribute to the SPGPQ capacity at a fractional ratio $x/(x - 1)$ of 1.1–1.9. While this ratio differs from the composite's molar ratio of 2.77 : 1 (see SI), it could reflect an underlying relationship between the electrochemical contributions and the composition. Furthermore, the performance enhancement factor ($y > 1$) is consistently observed across all cases, supporting the notion of synergy and the amplified performance of the composite.

To analyze the battery performance at different current densities, an RAB coin cell was cycled from 13 mA g^{-1} to 250 mA g^{-1} (see Fig. 8c). The battery exhibits the typical trend of decreasing capacity with increasing current density, as higher charging and discharging rates (*e.g.* 250 mA g^{-1}) result in kinetic limitations such as slower ion diffusion and increased polarization effects. Despite these challenges, the composite cathode sustained a capacity of 80 mAh g^{-1} at 50 mA g^{-1} after returning from 250 mA g^{-1}. The high coulombic efficiency of $(99 \pm 2)\%$, along with this capacity recovery, demonstrates the battery's impressive rate capability and reversibility. At the highest tested current density of 250 mA g^{-1}, the battery maintained a capacity of ≈ 51 mAh g^{-1}, retaining approximately 56% of its low-rate capacity (91 mAh g^{-1} at 13 mA g^{-1}). Moreover, the capacity recovery to 80 mAh g^{-1} at 50 mA g^{-1} and 68 mAh g^{-1} at 100 mA g^{-1} after the current density was reduced further suggests that the composite material remained stable during higher-rate cycling. This indicates that the capacity loss observed at higher rates is primarily due to kinetic limitations rather than irreversible damage to the battery.

Fig. 8d shows the cyclability of a solid polymer RAB with composite cathode at a current density of 210 mA g^{-1} for charging and 175 mA g^{-1} for discharging. The initial capacity was 61 mAh g^{-1}, which kept increasing over cycling and reached 122 mAh g^{-1} at cycle 1500 with a high coulombic efficiency of $(99 \pm 1)\%$. The capacity was not stable but rather had a zigzag trend. This continuously increasing trend in capacity along with the high efficiency indicates the system is probably undergoing some activation processes with a larger over-potential or environmental influences. This type of activation process during the initial charging and the gradual increase in capacity is also mentioned in the case of PQ composite with activated carbon.[22] In addition, the use of solid iono-polymer electrolytes may also crucially limit cathode wetting. This means, over the cycles more and more composite material becomes accessible to the electrolyte thereby increasing capacity. There is a small drop of capacity after the 35th cycle, which could be a result of a stabilization phase at the electrode–electrolyte interface, *i.e.* the system reaches a saturation state.

Other possible reasons could be unwanted side reactions with the moisture content present in the deeper layers of the cathodes or initial dissolution of PQ limited to a certain proportion. However, the consistent CE of 99% suggests that such unwanted reactions or dissolution are very limited. Apart from these, the ambient temperature can also be a critical parameter. An increasing pattern in $C_{cathode}$ during the day and a decreasing trend during the night (see the inset of Fig. 8d) suggest the vital role of temperature. It is important to note that the temperature increased from 22 °C to 31 °C during the cycling. An increase in temperature can enhance ion mobility and reduce cell resistance resulting in a capacity increase, however, the consistent and high coulombic efficiency ensures that there is no significant degradation inside the cell and the composite remains stable at least in a certain temperature range.

To verify the temperature sensitivity and identify the operating range, a temperature-controlled GCPL was carried out at

225 mA g^{-1}. For each temperature increase, there was a 2-hour resting period to allow the cell to adapt to the new temperature. There is a distinct trend of increasing capacity with increasing temperature suggesting that the system is severely sensitive to temperature. Fig. 8e shows that the initial capacity is around 40 mAh g^{-1}, which increases up to 53 mAh g^{-1} until the 35th cycle at room temperature. The observed trend could be attributed to enhanced cathode wetting with SPE, leading to improved accessibility of the solid electrolyte to the active material. The capacity reaches 90 mAh g^{-1} at 30 °C and 102 mAh g^{-1} at 35 °C following a consistent pattern due to enhanced ionic conductivity and improved electrode kinetics. Additionally, the increased fluidity of the SPE at elevated temperatures likely facilitates cathode wetting, enabling better utilization of the active material in the electrochemical reaction. C_{SPGPQ} returns to its initial value when the temperature is lowered back to room temperature further confirming the temperature sensitivity of the cell. The system maintains a high CE of (98 ± 2)% up to 35 °C, which indicates a high reversibility in this temperature range and the increased capacity does not come at the cost of efficiency. However, despite the high capacity at 40 °C, a gradual decrease in CE suggests the initiation of side reactions and irreversible material degradation. These parasitic side reactions are possibly attributed to thermal degradation of the PA6-based polymer electrolyte, the

onset of chemical decomposition of the PMMA binder, or partial dissolution of PQ under electrochemical stress at elevated temperatures. Upon returning to room temperature, the capacity reverted to its initial value; however, the persistent capacity fading signifies continued degradation. This observation indicates an optimal temperature limit of 35 °C and also confirms that the temperature influence was dominating while the cell was cycling (see Fig. 8d). In addition, the use of thermally stable solid polymer electrolytes, such as PAN-based systems[57] along with alternative binder additives and optimized graphite to PQ ratio, could help mitigate performance degradation at elevated temperatures (>35 °C).

2.4.3. Influence of the graphite shape. To analyze the shape dependency of the graphite host material on the composite cathode performance, different graphites, *i.e.* MCMB, GF, and SPG, were tried as hosts for the synthesis of composites using melt diffusion. Fig. 9a illustrates the CV curves of GFPQ, SPGPQ and MCMBPQ at 1 mV s^{-1}. All of the cathodes have almost identical curves with very similar peak shapes and positions. Although the specific current density of the SPGPQ peak is lower than for the other two, the patterns are similar. The specific capacity considering the integrated area of the SPGPQ (424 mA V g^{-1}) was also lower than for both GFPQ (510 mA V g^{-1}) and MCMBPQ (550 mA V g^{-1}). The variations can be attributed to the shape of the hosts and the process
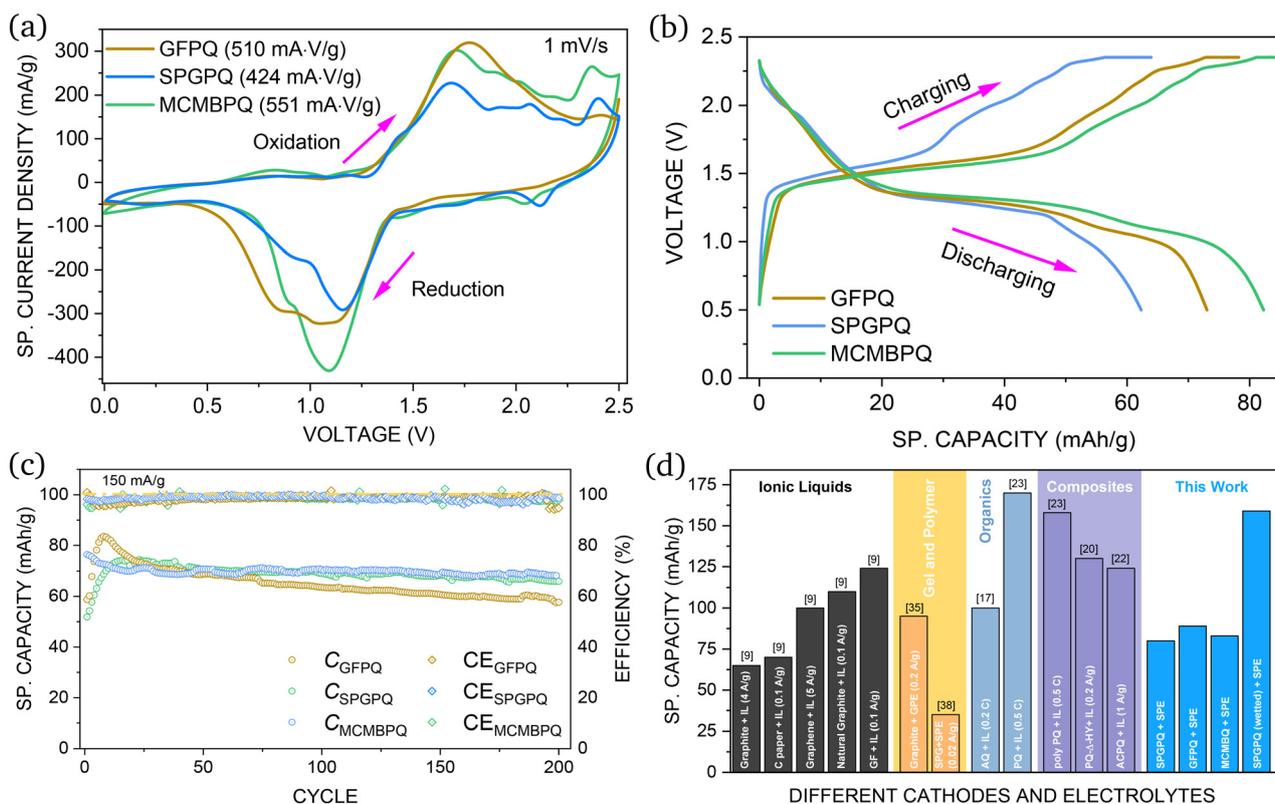

Fig. 9 Electrochemical performance of composite cathodes with different shapes of graphites: (a) comparison of CV curves, (b) Galvanostatic voltage profile of different composite cathodes at 50 mA g^{-1}, (c) total capacity and coulombic efficiency of the RABs with different cathodes and (d) a comparison of capacity between composites studied in this work and previously reported cathodes.

parameters. As mentioned earlier, the SPE may take some time to wet cathodes, which may vary from cell to cell.

The trend of increasing capacity observed in CV is also reflected in the charge–discharge voltage profile at a current density of 25 mA g^{-1} (see Fig. 9b). MCMBPQ offers the highest capacity of ≈84 mAh g^{-1} compared to GFPQ (79 mAh g^{-1}) and SPGPQ (63 mAh g^{-1}) after the 50th cycle. The plateaus during charging and discharging are also similar, indicating the improved performance of the composites regardless of the graphite type. However, when charging at a higher current density of 150 mA g^{-1}, the difference in capacities is reduced significantly with a promising CE (99 ± 4)% (see Fig. 9c). The influence of increased current density on SPGPQ is minimal, which can be attributed to its superior electrical conductivity of 1.36 S m^{-1} (see Table 1), facilitating faster electron transport and enabling more efficient electrical pathways. Table 1 presents the electrochemical performances of different composite cathodes. The capacity retention of all the composites is also improved up to 99% compared to pure PQ (70%) after 75 cycles (see Fig. S4a and S4b, SI). The energy density of the composite cathodes with SPE is also improved almost 100% compared to both PQ and SPG.

A comparison of the initial discharge capacities for cathode materials from this study and literature is presented in Fig. 9d. The composite cathodes synthesized in this work achieve capacities up to 90 mAh g^{-1} with SPE, and 160 mAh g^{-1} when wetted with an ionic liquid (IL). This performance confirms a significant improvement over conventional graphite cathodes paired with IL or SPE.

3. Conclusion

A composite consisting of PQ and graphite was synthesized using a simple one-step melt diffusion process for RABs, which was confirmed by several experimental observations, *i.e.* CBS, TGA, and XRD. The FTIR data analysis indicates that the composite is comparatively more stable than the pure PQ, while its electrical conductivity is nearly twice as high, demonstrating a significant improvement.

In the electrochemical reaction process, two different ionic species are involved, which are the intercalation of AlCl$_4^-$ into graphene layers during charging and coordination reactions between C=O and AlCl$_2^+$ during discharging with a high degree of reversibility. To verify this hypothesis, *operando* XRD, ATR-FTIR, XPS and EPR measurements were carried out. All of the analyses support the hypothesis that two different reaction mechanisms are taking place simultaneously with impressive reversibility. The CV curve analysis confirms the peak merging, which is also congruent with the other findings.

The overall battery capacity of the composite cathode with SPE is significantly improved by more than 70% compared to pure graphite and 82% compared to PQ, which is consistently reproduced with two other forms of graphite. The experimental data also suggest that the iono-polymer RABs with a composite cathode can operate without degradation up to a

temperature of 35 °C. All the composites can be cycled at a high current density of 250 mA g^{-1} with an exceptional coulombic efficiency of (99 ± 2)%. Overall, the composite has high potential as an active material for safe and high-performance iono-polymer RABs.

Author contributions

Shuvrodev Biswas contributed to the writing of the original draft, sample preparation and characterization, data processing, editing, investigation, and overall study design. Thomas Köhler was responsible for FT-IR and EPR investigations, data processing, editing, and experimental idea development. Amir Mohammad developed the electrolyte recipe and contributed to the research framework. Hartmut Stöcker participated in XRD analysis, review, editing, supervision, and project guidance. Dirk C. Meyer was involved in editing, validation, supervision, project administration, and funding acquisition.

Conflicts of interest

There are no conflicts to declare.

Data availability

Due to the large volume of calculation data in this paper and the data-sharing restrictions imposed by our institution, it is not possible to upload all datasets to a public repository. However, detailed experimental procedures, supplementary spectroscopic data, and essential electrochemical studies are provided in the Supplementary information (SI). Additional data may be made available upon reasonable request.

Supplementary information is available. See DOI: https://doi.org/10.1039/d5eb00054h.

Acknowledgements

References

1 B. Ng, P. T. Coman, E. Faegh, X. Peng, S. G. Karakalos, X. Jin, W. E. Mustain and R. E. White, *ACS Appl. Energy Mater.*, 2020, **3**, 3653–3664.

2 E. A. Olivetti, G. Ceder, G. G. Gaustad and X. Fu, *Joule*, 2017, **1**, 229–243.

3 R. Wang, H. Wang, H. Zhao, M. Yuan, Z. Liu, G. Zhang, T. Zhang, Y. Qian, J. Wang, I. Lynch and Y. Deng, *Energy Mater.*, 2023, **3**, 300040.

4 T. Leisegang, F. Meutzner, M. Zschornak, W. Münchgesang, R. Schmid, T. Nestler, R. A. Eremin, A. A. Kabanov, V. A. Blatov and D. C. Meyer, *Front. Chem.*, 2019, **7**, 268.

5 J. Tu, W.-L. Song, H. Lei, Z. Yu, L.-L. Chen, M. Wang and S. Jiao, *Chem. Rev.*, 2021, **121**, 4903–4961.

6 B. Zhang, W. Zhang, H. Jin and J. Wan, *ChemistrySelect*, 2023, **8**, e202204575.

7 X. Wen, Y. Liu, A. Jadhav, J. Zhang, D. Borchardt, J. Shi, B. M. Wong, B. Sanyal, R. J. Messinger and J. Guo, *Chem. Mater.*, 2019, **31**, 7238–7247.

8 C. Legein, B. J. Morgan, F. Fayon, T. Koketsu, J. Ma, M. Body, V. SarouKanian, X. Wei, M. Heggen, O. J. Borkiewicz, P. Strasser and D. Dambournet, *Angew. Chem., Int. Ed.*, 2020, **59**, 19247–19253.

9 E. Faegh, B. Ng, D. Hayman and W. E. Mustain, *Nat. Energy*, 2020, **6**, 21–29.

10 K. V. Kravchyk, S. Wang, L. Piveteau and M. V. Kovalenko, *Chem. Mater.*, 2017, **29**, 4484–4492.

11 S. Gu, H. Wang, C. Wu, Y. Bai, H. Li and F. Wu, *Energy Storage Mater.*, 2017, **6**, 9–17.

12 Y. Liu, S. Sang, Q. Wu, Z. Lu, K. Liu and H. Liu, *Electrochim. Acta*, 2014, **143**, 340–346.

13 Z. Li, B. Niu, J. Liu, J. Li and F. Kang, *ACS Appl. Mater. Interfaces*, 2018, **10**, 9451–9459.

14 M. Chiku, H. Takeda, S. Matsumura, E. Higuchi and H. Inoue, *ACS Appl. Mater. Interfaces*, 2015, **7**, 24385–24389.

15 S. K. Das, T. Palaniselvam and P. Adelhelm, *Solid State Ionics*, 2019, **340**, 115017.

16 B. Tan, S. Han, W. Luo, Z. Chao, J. Fan and M. Wang, *J. Alloys Compd.*, 2020, **841**, 155732.

17 Z. Huang, X. Du, M. Ma, S. Wang, Y. Xie, Y. Meng, W. You and L. Xiong, *ChemSusChem*, 2023, **16**, e202202358.

18 D. Kong, T. Cai, H. Fan, H. Hu, X. Wang, Y. Cui, D. Wang, Y. Wang, H. Hu, M. Wu, Q. Xue, Z. Yan, X. Li, L. Zhao and W. Xing, *Angew. Chem., Int. Ed.*, 2021, **61**, e202114681.

19 J. Bitenc, N. Lindahl, A. Vizintin, M. E. Abdelhamid, R. Dominko and P. Johansson, *Energy Storage Mater.*, 2020, **24**, 379–383.

20 D. J. Kim, D.-J. Yoo, M. T. Otley, A. Prokofjevs, C. Pezzato, M. Owczarek, S. J. Lee, J. W. Choi and J. F. Stoddart, *Nat. Energy*, 2019, **4**, 51–59.

21 D.-J. Yoo, M. Heeney, F. Glöcklhofer and J. W. Choi, *Nat. Commun.*, 2021, **12**, 2386.

22 D.-J. Yoo and J. W. Choi, *J. Phys. Chem. Lett.*, 2020, **11**, 2384–2392.

23 J. Bitenc, U. Koir, A. Vizintin, N. Lindahl, A. Krajnc, K. Pirnat, I. Jerman and R. Dominko, *Energy Mater. Adv.*, 2021, **2021**, 9.

24 J. Zhang, Y. Wu, M. Liu, L. Huang, Y. Li and Y. Wu, *Angew. Chem., Int. Ed.*, 2023, **62**, e202215408.

25 H. Xu, T. Bai, H. Chen, F. Guo, J. Xi, T. Huang, S. Cai, X. Chu, J. Ling, W. Gao, Z. Xu and C. Gao, *Energy Storage Mater.*, 2019, **17**, 38–45.

26 C. Xu, S. Zhao, Y. Du, Z. Wang and J. Zhang, *Mater. Lett.*, 2020, **275**, 128040.

27 F. Jach, M. Wassner, M. Bamberg, E. Brendler, G. Frisch, U. Wunderwald and J. Friedrich, *ChemElectroChem*, 2021, **8**, 1988–1992.

28 H. Sun, W. Wang, Z. Yu, Y. Yuan, S. Wang and S. Jiao, *Chem. Commun.*, 2015, **51**, 11892–11895.

29 M.-C. Lin, M. Gong, B. Lu, Y. Wu, D.-Y. Wang, M. Guan, M. Angell, C. Chen, J. Yang, B.-J. Hwang and H. Dai, *Nature*, 2015, **520**, 324–328.

30 J. Meng, X. Yao, X. Hong, L. Zhu, Z. Xiao, Y. Jia, F. Liu, H. Song, Y. Zhao and Q. Pang, *Nat. Commun.*, 2023, **14**, 3909.

31 J. Meng, X. Hong, Z. Xiao, L. Xu, L. Zhu, Y. Jia, F. Liu, L. Mai and Q. Pang, *Nat. Commun.*, 2024, **15**, 596.

32 X. Han, Y. Bai, R. Zhao, Y. Li, F. Wu and C. Wu, *Prog. Mater. Sci.*, 2022, **128**, 100960.

33 P. Meng, Z. Yang, J. Zhang, M. Jiang, Y. Wang, X. Zhang, J. Luo and C. Fu, *Energy Storage Mater.*, 2023, **63**, 102953.

34 Z. Yu, S. Jiao, S. Li, X. Chen, W. Song, T. Teng, J. Tu, H. Chen, G. Zhang and D. Fang, *Adv. Funct. Mater.*, 2018, **29**, 1806799.

35 Z. Liu, X. Wang, Z. Liu, S. Zhang, Z. Lv, Y. Cui, L. Du, K. Li, G. Zhang, M.-C. Lin and H. Du, *ACS Appl. Mater. Interfaces*, 2021, **13**, 28164–28170.

36 X.-G. Sun, Y. Fang, X. Jiang, K. Yoshii, T. Tsuda and S. Dai, *Chem. Commun.*, 2016, **52**, 292–295.

37 A. Mohammad, T. Köhler, S. Biswas, E. Brendler, B. Störr, H. Stöcker, F. O. R. L. Mertens and D. C. Meyer, *ACS Appl. Energy Mater.*, 2025, **8**, 2576–2587.

38 A. Mohammad, T. Köhler, S. Biswas, H. Stöcker and D. C. Meyer, *ACS Appl. Energy Mater.*, 2023, **6**, 2914–2923.

39 Z. Zhu, Y. Men, W. Zhang, W. Yang, F. Wang, Y. Zhang, Y. Zhang, X. Zeng, J. Xiao, C. Tang, X. Li and Y. Zhang, *eScience*, 2024, **4**, 100249.

40 S. S. Nair, T. Saha, P. Dey and S. Bhadra, *J. Mater. Sci.*, 2020, **56**, 3675–3691.

41 R. D. Knuth, F. A. Knuth, G. K. Maron, C. W. Raubach, M. L. Moreira, P. L. G. Jardim, N. L. V. Carreno, E. C. Moreira, A. Gündel, I. T. S. Garcia and S. S. Cava, *J. Solid State Electrochem.*, 2023, **28**, 2059–2070.

42 N. Lindahl, J. Bitenc, R. Dominko and P. Johansson, *Adv. Funct. Mater.*, 2020, **30**, 2004573.

43 G. A. Elia, N. A. Kyeremateng, K. Marquardt and R. Hahn, *Batteries Supercaps*, 2018, **2**, 83–90.

44 C.-J. Pan, C. Yuan, G. Zhu, Q. Zhang, C.-J. Huang, M.-C. Lin, M. Angell, B.-J. Hwang, P. Kaghazchi and H. Dai, *Proc. Natl. Acad. Sci. U. S. A.*, 2018, **115**, 5670–5675.

45 P. Bhauriyal, A. Mahata and B. Pathak, *Phys. Chem. Chem. Phys.*, 2017, **19**, 7980–7989.

46 F. Guo, Z. Huang, M. Wang, W.-L. Song, A. Lv, X. Han, J. Tu and S. Jiao, *Energy Storage Mater.*, 2020, **33**, 250–257.

47 M. Mao, Z. Yu, Z. Lin, Y.-S. Hu, H. Li, X. Huang, L. Chen, M. Liu and L. Suo, *J. Mater. Chem. A*, 2020, **8**, 23834–23843.

48 G. Baruah, D. Tripathi and S. Nath, *Curr. Sci.*, 1970, **39**, 405–407.

49 P. Pal, H. Li, R. AlAjeil, A. K. Mohammed, A. Rezk, G. Melinte, A. Nayfeh, D. Shetty and N. ElAtab, *Adv. Sci.*, 2024, **11**, 2408648.

50 F. A. Stevie and C. L. Donley, *J. Vac. Sci. Technol., A*, 2020, **38**, 063204.

51 J. Stankowski, L. Piekara-Sady, W. Kempiski, O. Huminiecki and P. B. Sczaniecki, *Fullerene Sci. Technol.*, 1997, **5**, 1203–1217.

52 J. Wang, J. Polleux, J. Lim and B. Dunn, *J. Phys. Chem. C*, 2007, **111**, 14925–14931.

53 J. Yao, Y. Li, R. Huang, J. Jiang, S. Xiao and J. Yang, *Ionics*, 2020, **27**, 65–74.

54 Y. Yao, L. Zhang, Y. Gao, G. Chen, C. Wang and F. Du, *RSC Adv.*, 2018, **8**, 2958–2962.

55 F. Gan, K. Chen, N. Li, Y. Wang, Y. Shuai and X. He, *Ionics*, 2019, **25**, 4243–4249.

56 J. Shi, J. Zhang and J. Guo, *ACS Energy Lett.*, 2019, **4**, 2124–2129.

57 M. M. Rahman, M. J. Rana, S. Biswas, A. Mohammad, H. Stöcker and D. C. Meyer, *J. Power Sources*, 2025, **641**, 236776.